



# Analysis of thermal-mechanical causes of abrasive belt grinding for titanium alloy

Kangkang Song<sup>1,2</sup> · Guijian Xiao<sup>1,2</sup> · Shulin Chen<sup>1,2</sup> · Shaochuan Li<sup>1,2</sup>

Received: 2 December 2020 / Accepted: 8 February 2021 / Published online: 1 March 2021  
© The Author(s), under exclusive licence to Springer-Verlag London Ltd. part of Springer Nature 2021

## Abstract

The abrasive belt grinding process is a highly nonlinear dynamic change process. The coupling action mechanism between mechanical field and thermal field during grinding is complex and variable. In this paper, firstly, the abrasive belt grinding experiment of titanium alloy was carried out to measure the change of temperature and force during the grinding process, and the Savitzky-Golay filter analysis was carried out on force signal. Secondly, the generation of grinding heat and force was described in detail, the equilibrium process of thermal-mechanical coupling was analyzed, and the finite element equation of thermal-mechanical coupling was deduced for abrasive belt grinding. Thirdly, the finite element simulation model of abrasive belt grinding is established to comprehensively analyze the change rule of thermal-mechanical coupling in the grinding process. Finally, the experimental results and simulation results of belt grinding are discussed and analyzed. The experimental results found that the grinding force changes are divided into three different stages, and the maximum surface temperature decreases to a certain extent with the grinding process. The simulation results show that the plastic deformation zone and “dead metal zone” are consistent with the theory in the grinding process. This study can provide a reference for relevant machining and further improve the grinding workpiece’s surface quality through thermal-mechanical optimization.

**Keywords** Titanium alloy · Abrasive belt grinding · Thermal-mechanical coupling · Grinding experiment · Finite element simulation

## Nomenclature

$E_Q$	Total heat generated by grinding	$\alpha$	Ratio of frictional heat to thermal energy conversion
$Q_p$	Heat generated by the plastic deformation of the processed material	$R_1$	Ratio of thermal energy transfer to the abrasive belt grain-wear debris surface
$Q_f$	Heat generated by the mutual squeeze friction between the wear debris and the rake face of the abrasive belt grain, and the grinding surface and the top of the abrasive belt grain	$R_2$	Ratio of thermal energy transfer to the abrasive belt grain-workpiece surface
$Q_d$	Heat taken away by the wear debris	$P_{fr}$	Power of grinding heat generated by friction
$Q_a$	Heat taken away by the abrasive belt grains	$\tau$	Shear stress generated by friction
$Q_w$	Heat transferred by the processed material	$\gamma$	Relative slip rate of the contact surface
$Q_m$	Heat taken away by the surrounding medium	$\Delta s$	Slip distance
		$\Delta t$	Slip time
		$Q_A$	Heat transferred by friction in A direction
		$Q_B$	Heat transferred by friction in B direction
		$Q_1$	Transferred to the interior on the A surface
		$Q_2$	Transferred to the interior on the B surface
		$Q_k$	Energy lost due to the heat conduction
		$\vec{q}$	Heat flow vector
		$\vec{J}$	Entropy flux vector
		$d\varepsilon$	Total incremental strain
		$\rho h$	Time change rate of specific enthalpy per unit volume
		$[D^e]$	Stress-strain matrix of the elastic deformation

✉ Guijian Xiao  
xiaoguijian@cqu.edu.cn

<sup>1</sup> College of Mechanical Engineering, Chongqing University, No.174, Shazhengjie, Shapingba, Chongqing 400044, China

<sup>2</sup> The State Key Laboratory of Mechanical Transmissions, No.174, Shazhengjie, Shapingba, Chongqing 400044, China

$\bar{\sigma}$	Effective stress
$\bar{\varepsilon}$	Effective strain rate
$R$	Contact wheel radius
$h_s$	Height of the abrasive belt grain
$D$	Distance between the abrasive belt grains
$\varphi$	Angular displacement of the abrasive belt grain
$Q_r$	Energy lost due to the heat radiation
$k(h, p, \bar{\theta})$	Heat conductivity coefficient during the grinding process
$h$	Contact interference
$p$	Contact pressure
$\bar{\theta}$	Average temperature
$\varepsilon^T$	Strain caused by thermal extension
$C$	Measure the contact surface radiation
$\bar{q}$	Mises or Hill equivalent stress
$\theta_1$	Temperature of contact surface A
$\theta_2$	Temperature of contact surface B
$D(\theta)$	Material parameter related to temperature
$\theta^z$	Absolute zero value corresponding to the temperature unit used
$r^p$	Heat generated by the plastic strain per unit volume
$\eta$	Plastic heat generation rate
$\sigma$	Plastic stress
$\varepsilon^p$	Plastic strain rate
$\Delta t$	Time interval of each incremental step
$\Delta \varepsilon^p$	Plastic strain increment
$\vec{n}$	Heat flow direction matrix
$W$	Strain energy density
$\varepsilon$	Total strain
$\varepsilon^e$	Elastic strain
$\varepsilon^p$	Plastic strain
$d\varepsilon^e$	Elastic strain differential
$d\varepsilon^p$	Plastic strain differential
$d\varepsilon^T$	Thermal extension strain differential
$\rho s'$	Time change rate of specific entropy per unit volume
$R_s$	Radius of the cutting circle
$\bar{\varepsilon}$	Effective strain
$T$	Temperature
$d_b$	Thickness of the belt base
$v_s$	Abrasive belt linear speed
$v_w$	Abrasive belt linear speed
$\pm$	Up grinding and down grinding

## 1 Introduction

Titanium alloy as the key constituent material of aircraft engine core parts has the typical characteristics of difficult processing and the traditional machining methods are difficult to meet due to the requirements of its high surface integrity

[1–3]. Abrasive belt grinding is a kind of both material removal and the flexibility of polishing grinding, which is more efficient than the traditional grinding wheel, and a cold effect concurrently is one method commonly used in precision and ultra-precision machining titanium alloy [4–6]. In the process of abrasive belt grinding, there is a variety of physical field coupling phenomenon, of which the thermal field and mechanical field coupling are essential for the study of the mechanism and application of abrasive belt grinding [7, 8]. However, there are few reports on the thermal-mechanical coupling study of abrasive belt grinding. In the traditional machining process, the mechanical field and thermal field affect surface quality and part deformation is also applicable to grinding process [9–12]. The related knowledge helps study and understand the thermal-mechanical coupling process of grinding, but it is not the same. In the past, there have been many reports on thermal-mechanical coupling.

The thermal-mechanical coupling theory is the basis for the research of machining processes, and it is also the key to solving many engineering problems. Aiming at the effect of the combined effects of heat and force on the feed mechanism of CNC machine tools, Liu et al. [13] proposed a thermal-mechanical coupling dynamic analysis method combining multi-step finite element (FE) simulation and temperature field, which the verified correctness of the proposed method. Aiming at the characteristics of the complex load and multiple heat sources of the dual-drive feed system, Huang et al. [14] analyzed the effect of thermal-mechanical coupling on the dynamic performance and structural deformation of the feed system through experiments. They proved the rationality and feasibility of the thermal-mechanical coupling dynamic simulation analysis method. Aiming at the metal flow behavior of the cast slab at high temperature, Wu et al. [15] established a three-dimensional thermal-mechanical coupling model of two pairs of rolls based on the constitutive equation derived from the stress-strain curve at different temperatures and strain rates and verified its accuracy through experiments. Aiming at the problems of heat transfer and mechanical deformation in the industrial continuous casting billet mold, Chakraborty et al. [16] analyzed the temperature field and stress field in the mold and the resulting deformation and determined the optimal taper of the mold according to the deformation curve of the mold and the heat shrinkage rate of the billet. Aiming at the thermal-mechanical simulation problem of friction stir welding, Soundararajan et al. [17] established a FE thermal-mechanical model of the tool load with force considering the uniform value of contact conductance. They predicted the stress at the interface between the workpiece and the backplate and the thermal history of the workpiece.

In recent years, many scholars have researched the related prediction of thermal-mechanical coupling. In order to

accurately predict the impact of the local friction process, Wang et al. [18] proposed a thermal-mechanical coupling simulation method based on geometric compression tools, which proved the effectiveness of the method from theoretical and experimental comparisons. Aiming at the thermal-mechanical coupling problem in the micro-milling process, Lu et al. [19] proposed a micro-milling model considering the temperature and force, predicted the micro-milling force and temperature, and verified the accuracy of the proposed method. In order to study the thermal stress distribution of disk cutters, Zhang et al. [20] conducted dynamic simulation and mechanical analysis on the rock breaking process of disk cutters, and the simulation results reflected the distribution of thermal stress. In order to realize the overall manufacture of TC4 large titanium alloy parts, Jiang et al. [21] used thermal-electric coupling and thermal-mechanical coupling methods to predict temperature changes and sheet deformation behavior. They proved that this method could calculate the power-assisted incremental process. In order to study the influence of bearing structure on the thermodynamic behavior of high-speed spindles, Li et al. [22] established a comprehensive dynamic thermodynamic model and coupled the thermal model with the dynamic spindle model. They explained the effects of different bearing structures on the thermal and dynamic characteristics of the spindle.

The thermal-mechanical coupling caused by different processing methods has always been the concern of many scholars. Aiming at the thermal-mechanical coupling problem in the steel plate welding process, Farias et al. [23] used ANSYS software to conduct mechanical and thermal simulations on the material properties of Gaussian distribution, and the results were in agreement with the experimental results. Aiming at the high strength-to-weight ratio of heat-resistant high-entropy alloys, Zhang et al. [24] used the finite difference (FD) method and FE method to couple the temperature and thermal stress distribution of continuous selective laser melting (SLM) process. It was proved that the thermal model and the mechanical model combined with the FD-FE method can simulate and improve the entire SLM process. In order to realize the thermal-micro-mechanical simulation of the metal forming process, Motaman et al. [25] added a microstructure solver to the built-in thermal and force solver of the standard FE package and realized the thermal-micro-mechanical coupling simulation of the cold and hot metal forming process. Aiming at the thermal-mechanical coupling problem of the titanium alloy forming process, Ji et al. [26] used Deform-3D to analyze the metal flow, temperature, stress, and strain distribution during the forming process and verified the Ti-6Al-4V blade on the H500 CWR rolling mill. In order to study the thermodynamic properties of the plasma sprayed NiCrBSi coating, Liu et al. [27] used the transient temperature of each node as the thermal load and calculated the deformation and stress state of the specimen. The results showed that the

quenching stress dominates the final residual stress in the coating.

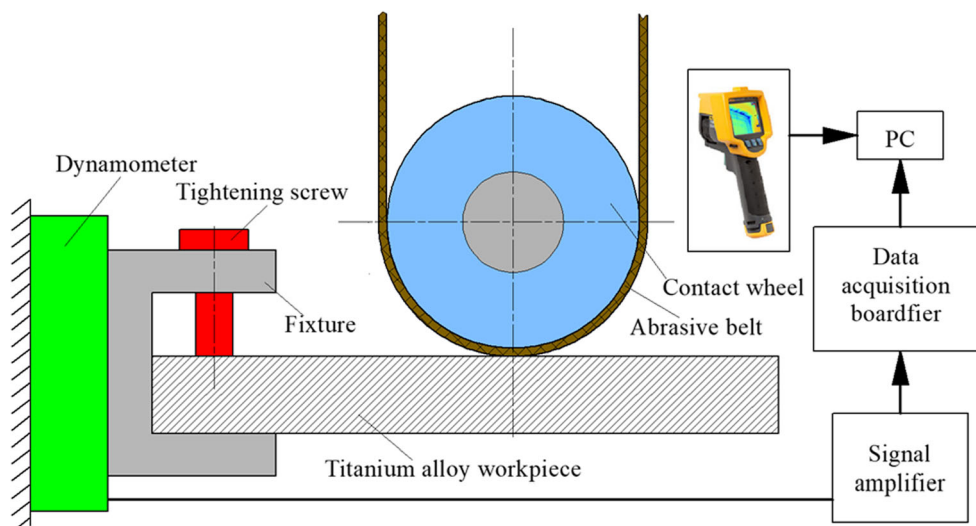
Unlike traditional thermal-mechanical couplings such as cutting, welding, and metal thermoforming, abrasive belt grinding is a highly nonlinear process because of its flexible machining and small machining allowance. Simultaneously, the coupling mechanism between the mechanical field and thermal field is complex and changeable during processing. So far, the research on thermal-mechanical coupling of abrasive belt grinding has been relatively macro, and the research of thermal-mechanical coupling in the grinding process on surface integrity is still in the initial exploration stage [28]. Therefore, the titanium alloy abrasive belt grinding experiment is carried out, and the change of temperature and force is measured during the grinding process in Section 2. In Section 3, the generation of grinding heat and force was explained, the equilibrium process of thermal-mechanical coupling is analyzed, and the grinding thermal-mechanical coupling FE equation is deduced; A FE simulation model is established for abrasive belt grinding, and the change law of thermal-mechanical coupling is analyzed during the grinding process in Section 4. Experiments and simulations of abrasive belt grinding are discussed in Section 5. Finally, the conclusion of this study is given.

## 2 Thermal-mechanical experiment of abrasive belt grinding

### 2.1 Experimental principle and method

Grinding temperature is the focus of thermal-mechanical coupling research. Its accurate measurement plays an important role in judging the correctness of the coupling model. During the grinding process, a handheld infrared thermal imager is used to detect the surface temperature of the workpiece, which can realize the automatic alignment of visible light image and infrared light image and then accurately record the surface temperature of the grinding. The measurement of the grinding force adopts the resistance strain measurement method. The dynamometer is fixed on the worktable. The two ends of the fixture are connected with the dynamometer and the workpiece. The workpiece to be grinding is fixed on the fixture. When grinding, under the grinding force's action, the deformation structure of the measuring platform in the three directions of XYZ deforms accordingly. The three sets of resistance strain gauges fixed on the deformation structure convert the deformation in each direction into corresponding voltage changes and the parameters corresponding to the output grinding force. The principle is shown in Fig. 1.

**Fig. 1.** Schematic diagram of experimental measurement



The test adopts the method of surface grinding. The titanium alloy TC4 is used as the test material. The chemical composition and mechanical properties at room temperature (25 °C) are shown in Table 1 and Table 2, respectively. The 240# pyramid alumina abrasive belt is used as a grinding tool. The abrasive belt grinding speed is 10 m/s, the feed speed is 60 mm/min, and the grinding depth is 30 μm. The dynamometer model is FC3D80, and the thermal imager model is Fluke TiR32. The technical parameters of the dynamometer are shown in Table 3. During the test, the grinding force and the surface temperature of the workpiece are measured simultaneously, as shown in Fig. 2.

## 2.2 Experimental analysis of abrasive belt grinding

### 2.2.1 Experimental analysis of grinding force

Grinding force is a constantly changing physical quantity in the grinding process. As a continuous signal, some high-frequency noise will appear due to the jitter of the abrasive belt and signal interference during measurement. Currently, it is necessary to select the corresponding low-pass filter to process the grinding force signal to obtain smoother data, which is convenient for

subsequent regular observation and value reading and records the value of the grinding force in the *x* and *y* directions during the grinding process. The data acquisition board obtains the grinding force’s change from elasticity to plasticity by reading the continuous grinding force signal from the resistance strain dynamometer. The original signal is processed twice by MATLAB. The Savitzky-Golay filter can better retain the details and characteristics of the original signal. Therefore, the Savitzky-Golay filter method is used to filter the grinding force original signal. In the MATLAB algorithm, the value of framelen is 1501. The result is shown in Fig. 3.

Figure 3 (a) and (b) show the original signal data and the Savitzky-Golay filtered signal data of the grinding force in the *x* direction, respectively. It can be clearly seen from the signal filtered by Savitzky-Golay that the zone I is in the grinding contact stage, and the grinding force fluctuates greatly in the *x* direction. Zone II is in the grinding stable stage, and the grinding force is relatively stable in the *x* direction, about 6.1 N. Zone III is in the grinding exit stage, and the grinding force fluctuates greatly in the *x* direction, but it eventually tends to a smaller stable value. Figure 3(c) and (d) show the original signal data and the Savitzky-Golay filtered signal data of the grinding force in the *y* direction, respectively. Zone I is in the grinding contact stage,

**Table 1** Chemical composition of TC4 workpiece [29]

Element	Al	V	Fe	C	N	H	O	Ti
Content (wt%)	5.5 ~ 6.8	3.5 ~ 4.5	≤ 0.3	≤ 0.1	≤ 0.05	≤ 0.015	≤ 0.2	Bal

**Table 2** Mechanical properties of TC4 workpiece [29]

Category	Elasticity modulus (GPa)	Density (kg/m <sup>3</sup> )	Yield strength (MPa)	Tensile strength (MPa)
Parameter value	111.5	4640	1110	≥ 895



**Table 3** Technical parameters of dynamometer

Parameter index	Reference value
Range	100 N
Sensitivity (Fx/Fy/Fz)	0.5 ~ 1.5 mV/V
Nonlinear error	< 0.15 %F.S.
Hysteresis error	< 0.25 %F.S.
Zero temperature effect	< 0.05 %F.S./10 °C
Maximum excitation voltage	15 VDC
Operating temperature range	- 30 ~ + 75 °C
Elastomer material	40 CrMo alloy steel

and the grinding force fluctuates greatly in the  $y$  direction (whether it is Fig. 3(c) or Fig. 3(d)). Zone II is in the grinding stable stage, and the grinding force is relatively stable in the  $y$  direction, about 2.8 N. Zone III is in the grinding exit stage, and the grinding force fluctuates greatly in the  $y$  direction, but it eventually tends to a smaller stable value.

In summary, due to the jitter of the abrasive belt and the signal's interference, the grinding force fluctuates greatly in the grinding contact stage of zone I and the grinding exit stage of zone III. In the grinding stable stage of zone II, the value of the grinding force is relatively stable. This is different from the research in literature [30], which divides the grinding into an idling stage and a grinding stage and does not give a specific grinding force.

### 2.2.2 Experimental analysis of grinding temperature

The surface temperature of the grinding process is recorded by an infrared thermal imager. The surface temperatures at the beginning of the grinding  $t = 5$  s, the middle of the grinding  $t = 35$  s, and the later of the grinding  $t = 60$  s were recorded. The whole process is shown in Fig. 4.

Figure 4(a1) is the full infrared image of the grinding at  $t = 5$  s. Since the grinding has just started, the bright area of the temperature is small. It can be seen that the highest temperature of the grinding surface is 52.95 °C at this time. Figure 4(a2) is the full

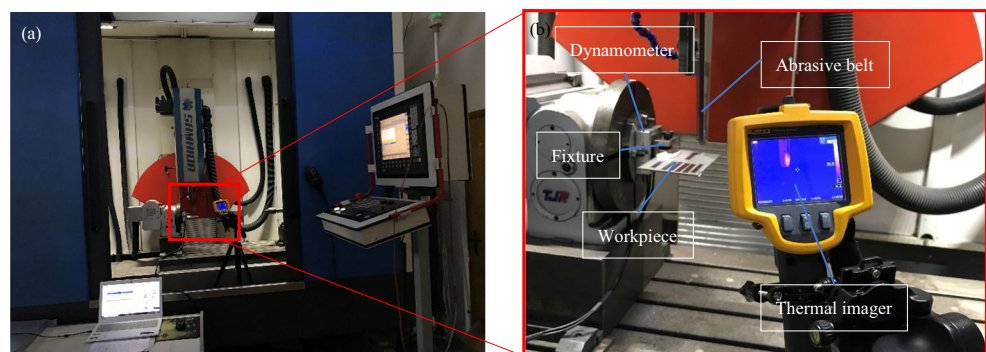
visible light image at this time, and it can be seen that the grinding has just started. Figure 4(a3) shows the three-dimensional distribution of the grinding temperature in the field of view at this time. It can be seen that the peak in the middle of the temperature distribution is more consistent with Fig. 4(a1). The temperature around the peak temperature gradually decreases until it drops to room temperature 33.2 °C.

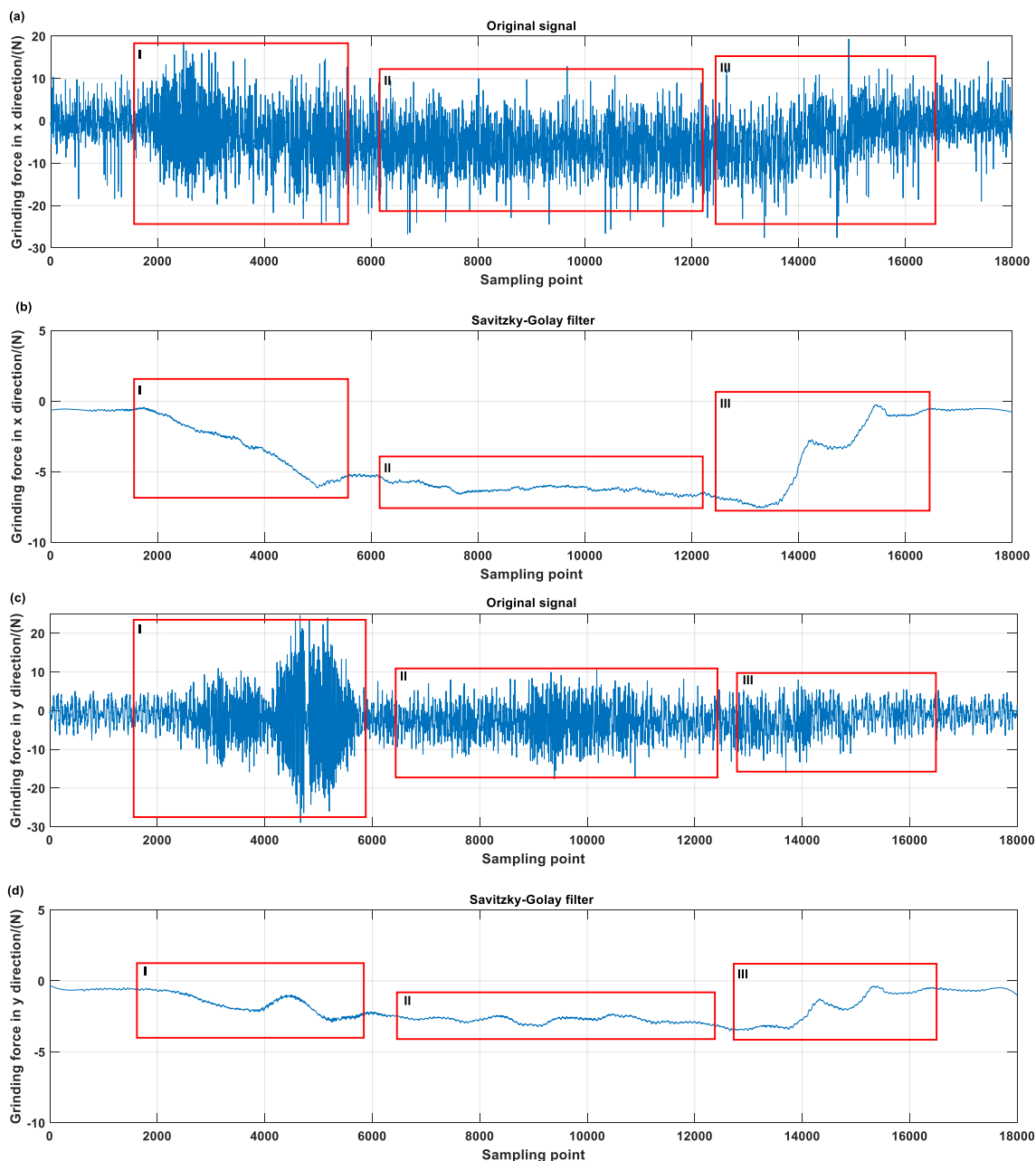
Figure 4(b1) is the full infrared image of the grinding at  $t = 35$  s. It can be seen that the highest temperature of the grinding surface is 49.38 °C at this time, and the bright area of temperature is larger than that of Fig. 4(a1). Figure 4(b2) is the full visible light image at this time, and it can be seen that the grinding has been carried out about half. Figure 4(b3) shows the three-dimensional distribution of the grinding temperature in the field of view at this time. It can be seen that the peak in the middle of the temperature distribution is more consistent with Fig. 4(b1). The temperature around the peak temperature gradually decreases until it drops to room temperature 33.2 °C.

Figure 4(c1) is the full infrared image of the grinding at  $t = 60$  s, it can be seen that the highest temperature of the grinding surface is 43.30 °C, and the bright area of the temperature is further expanded. Figure 4(c2) is the full visible light image at this time; it can be seen that the grinding is basically completed. Figure 4(c3) shows the three-dimensional distribution of the grinding temperature in the field of view at this time. It can be seen that the peak in the middle of the temperature distribution is more consistent with Fig. 4(c1). The temperature around the peak temperature gradually decreases until it drops to room temperature 33.2 °C.

In summary, from Fig. 4(a1)→(b1)→(c1), the bright area of the grinding temperature gradually increases, which indicates that the heat-affected zone by the temperature increases as the grinding progresses. This phenomenon is more consistent with the law described in the literature [27]. In addition, the temperature of the abrasive belt and the contact wheel also increased to a certain extent. From Fig. 4(a3)→(b3)→(c3), the bulge in the upper left corner becomes higher and higher, which indicates that the temperature has accumulated and affects the surrounding fixture temperature as the grinding progresses. There are similar conclusions in literature [31].

**Fig. 2** (a) Overall view of the experimental setup; (b) partially enlarged view of the experimental setup





**Fig. 3** (a) Original signal data of grinding force in  $x$  direction; (b) Savitzky-Golay filtered signal data of grinding force in  $x$  direction; (c) original signal data of grinding force in  $y$  direction; (d) Savitzky-Golay filtered signal data of grinding force in  $y$  direction

### 3 Thermal-mechanical coupling theory of abrasive belt grinding

#### 3.1 Generation of force and heat in abrasive belt grinding

##### 3.1.1 Generation of grinding force

During the grinding process, abrasive belt grains cut into the workpiece, so that the grinding layer becomes wear debris and flows out along the belt linear speed and the grinding surface is obtained at the same time. It not only needs to overcome the

force that causes the workpiece material to produce shear deformation but also needs to overcome the internal frictional resistance that occurs on the contact surface between the abrasive belt grains and the workpiece. Therefore, the forces are mainly dispersed in the I, II, and III deformation zones in the grinding process. As shown in Fig. 5, the main sources of grinding force are as follows:

- (1) Overcome the elastic pressure  $F_{e1}$ ,  $F_{e2}$  generated by the elastic deformation of metal materials during the grinding process.

**Fig. 4** (a1) Full infrared image of grinding at  $t = 5$  s. (a2) Full visible light image of grinding at  $t = 5$  s. (a3) Three-dimensional distribution of the grinding temperature in the field of view at  $t = 5$  s. (b1) Full infrared image of the grinding at  $t = 35$  s. (b2) Full visible light image of grinding at  $t = 35$  s. (b3) Three-dimensional distribution of grinding temperature in the field of view at  $t = 35$  s. (c1) Full infrared image of grinding at  $t = 60$  s. (c2) Full visible light image of grinding at  $t = 60$  s. (c3) Three-dimensional distribution of the grinding temperature in the field of view at  $t = 60$  s

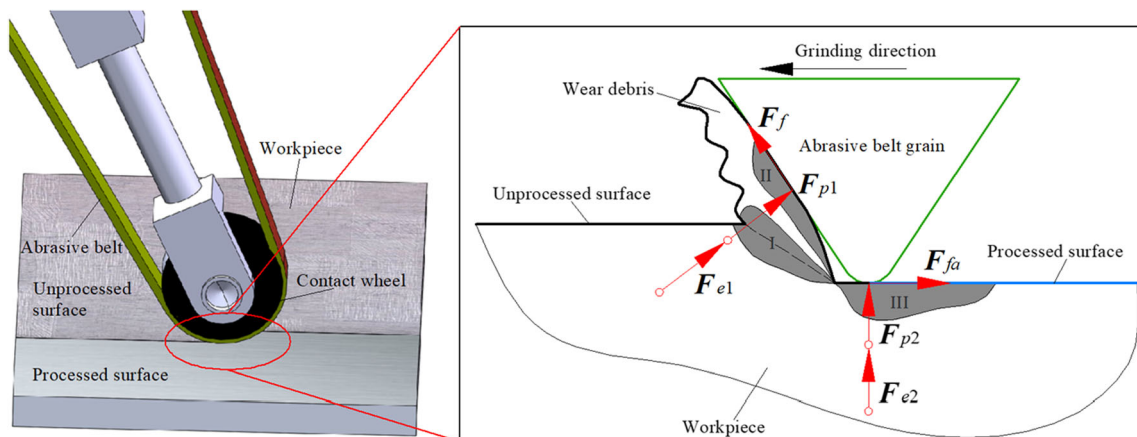
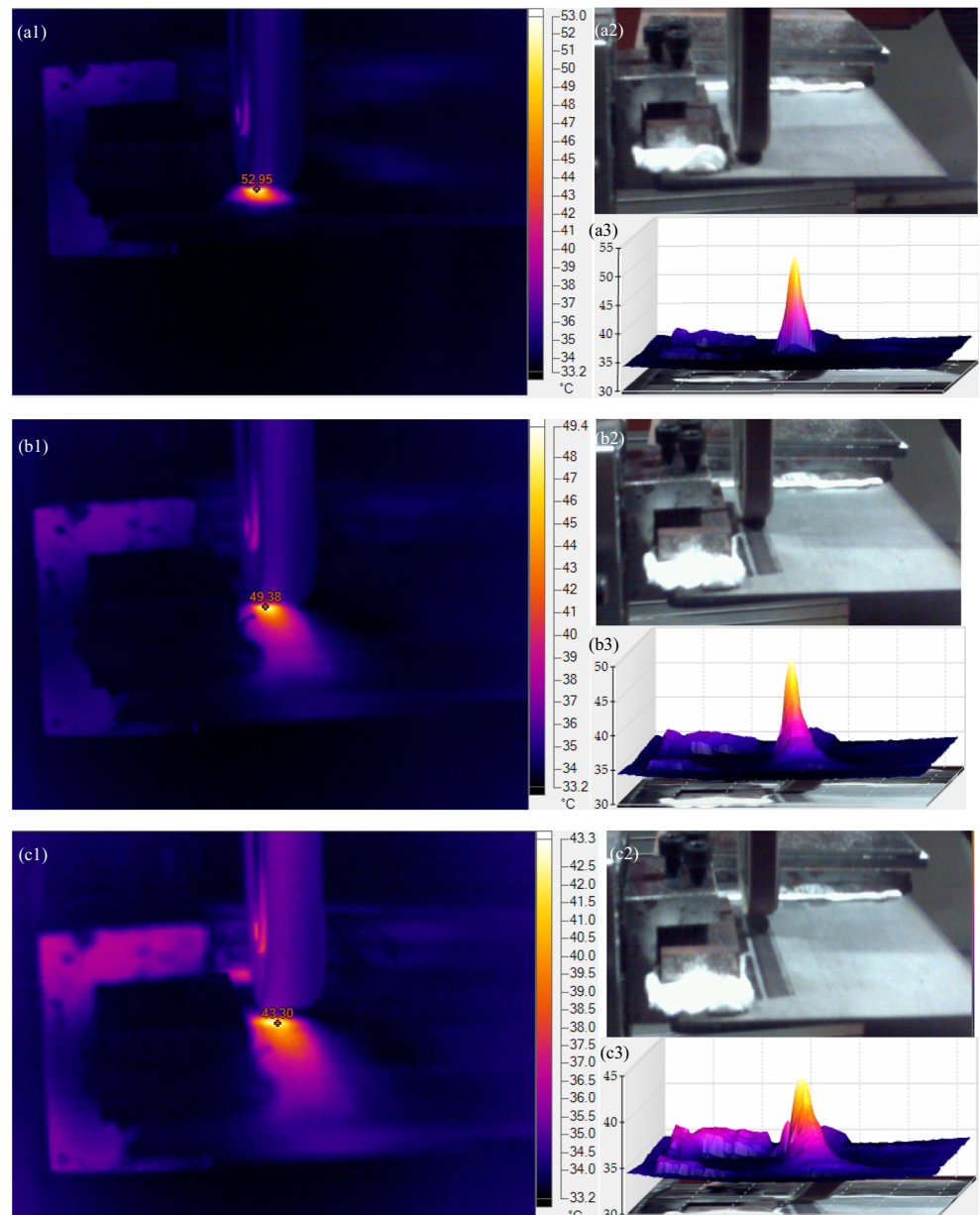


**Fig. 5** Source of grinding force

- (2) Overcome the plastic pressure  $F_{p1}$ ,  $F_{p2}$  generated by the plastic deformation of the metal material during the grinding process.
- (3) Overcome the frictional force  $F_f$  generated between the wear debris and the rake face of the abrasive belt grain and the frictional force  $F_{fa}$  generated between the grinding surface and the top of the abrasive belt grain.

In order to facilitate the study, these scattered forces are grouped together and represented by the total grinding force  $F$ . The study of total grinding force is very important. It can not only be used to calculate the grinding power but also provide important and reliable standards in the design and selection of machine tools, fixtures, and abrasive tools.

### 3.1.2 Generation of grinding heat

As abrasive belt grains continuously cut into the material to be processed, the material undergoes elastoplastic deformation under the action of abrasive belt grains, and the energy consumed in this process is basically converted into grinding heat. In addition, the friction between the wear debris, the grinding surface of the workpiece, and the abrasive belt grains will also consume a part of the energy, thus generating the corresponding heat. In the process of abrasive belt grinding of metal, the energy consumed is mainly converted into grinding heat. As shown in Fig. 6, the heating area mainly comes from the three deformation areas of grinding. Another part of the heat comes from the mutual squeeze friction between the wear debris and the rake face of the abrasive belt grain and the grinding surface and the top of the abrasive belt grain.

According to the thermodynamic equilibrium principle, the amount of grinding heat generated and the amount of grinding heat diffused should be consistent during the grinding process, as expressed in Eq. (1):

$$E_Q = Q_p + Q_f = Q_d + Q_a + Q_w + Q_m \quad (1)$$

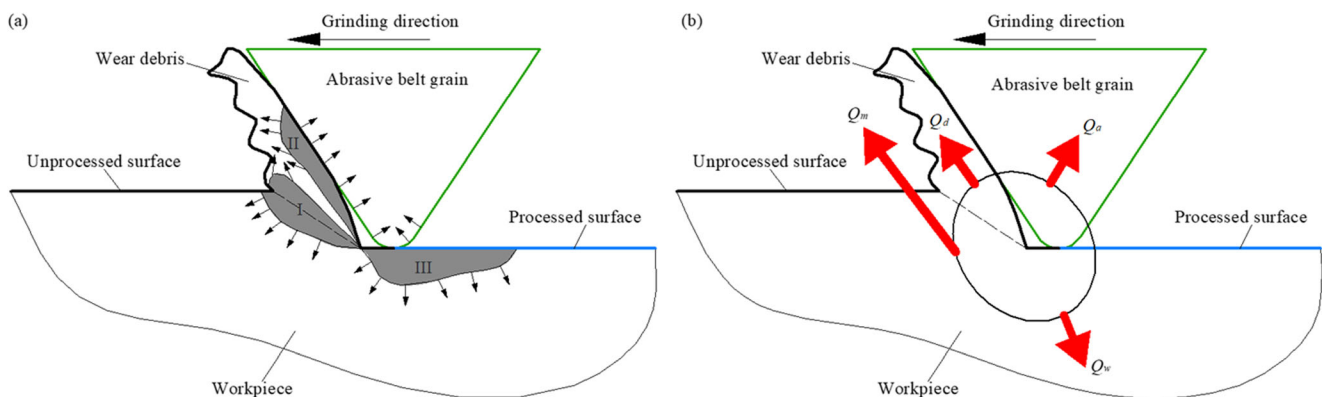


Fig. 6 (a) Source of grinding heat; (b) transmission of grinding heat

where  $E_Q$  is the total heat generated by grinding,  $Q_p$  is the heat generated by the plastic deformation of the processed material,  $Q_f$  is the heat generated by the mutual squeeze friction between the wear debris and the rake face of the abrasive belt grain and the grinding surface and the top of the abrasive belt grain,  $Q_d$  is the heat taken away by the wear debris,  $Q_a$  is the heat taken away by the abrasive belt grains,  $Q_w$  is the heat transferred by the processed material, and  $Q_m$  is the heat taken away by the surrounding medium, such as air, grinding fluid, etc.

**(1) Frictional heat generating process** During the grinding process, with the continuous friction between the wear debris and the rake face of the abrasive belt grain, and the grinding surface and the top of the abrasive belt grain, the frictional force continues to do work and generates frictional heat with a certain conversion efficiency. The ratio of frictional heat to thermal energy conversion is set to  $\alpha$ , the ratio of thermal energy transfer to the abrasive belt grain-wear debris surface and the abrasive belt grain-workpiece surface respectively is  $R_1$  and  $R_2$ , and the sum of  $R_1$  and  $R_2$  is the complete thermal efficiency. The setting of  $R_1$  and  $R_2$  is based on the contact surface which has no heat absorption and loss, and the energy can only be conducted through thermal conduction to abrasive belt grains, wear debris, and workpiece, or diffused outward through thermal radiation.

The power of grinding heat generated by friction can be calculated by Eq. (2) [32]:

$$P_{fr} = \tau \cdot \dot{\gamma}, \dot{\gamma} = \frac{\Delta s}{\Delta t} \quad (2)$$

where  $\tau$  is the shear stress generated by friction,  $\dot{\gamma}$  is the relative slip rate of the contact surface, and  $\Delta s$  and  $\Delta t$  are the slip distance and time in an incremental step, respectively.

According to the definition of the transfer ratio, the heat flowing to the two contact surfaces is expressed as Eq. (3):



$$\begin{cases} Q_A = R_1 \cdot \alpha \cdot P_{fr} \\ Q_B = R_2 \cdot \alpha \cdot P_{fr} \end{cases} \quad (3)$$

where  $Q_A$  and  $Q_B$  represent the heat transferred by friction in two directions, respectively. Since the heat generated by friction will heat up to different degrees on different contact surfaces, heat conduction and heat radiation also exist on the contact surfaces, and there will be a certain amount of heat loss. Therefore, while assuming the heat transfer on the A and B surfaces, considering the heat dissipated, the heat  $Q_1$  and  $Q_2$  finally transferred to the interior are expressed as Eq. (4):

$$\begin{cases} Q_1 = Q_A - Q_k - Q_r \\ Q_2 = Q_B - Q_k - Q_r \end{cases} \quad (4)$$

where  $Q_k$  and  $Q_r$  are the energy lost due to the heat conduction and heat radiation of the contact surface, which can be determined by the thermal conductivity coefficient of the contact surface, is expressed as Eq. (5):

$$\begin{cases} Q_k = k(h, p, \bar{\theta})(\theta_1 - \theta_2) \\ Q_r = C[(\theta_1 - \theta^z)^4 - (\theta_2 - \theta^z)^4] \end{cases} \quad (5)$$

where  $k(h, p, \bar{\theta})$  is the heat conductivity coefficient during the grinding process, which is related to the contact interference  $h$ , contact pressure  $p$ , and average temperature  $\bar{\theta}$ ,  $C$  is a constant that measure the contact surface radiation,  $\theta_1$  and  $\theta_2$  are the temperatures of two contact surfaces, respectively, while  $\theta^z$  is the absolute zero value corresponding to the temperature unit used.

**(2) Plastic deformation heat generation process** In the abrasive belt grinding process, in addition to the heat generated between the wear debris, the workpiece, and the abrasive belt grains, the material will also generate heat when subjected to the grinding force and plastic deformation to form wear debris. In the analysis process, the heat generated by the plastic strain per unit volume can be set as Eq. (6) [33]:

$$r^p = \eta\sigma/\dot{\varepsilon}^p = \frac{1}{2\Delta t}\eta\Delta\varepsilon^p \vec{n}/(\sigma + \sigma_t) \quad (6)$$

where  $\eta$  is the plastic heat generation rate,  $\sigma$  is the stress,  $\dot{\varepsilon}^p$  is the plastic strain rate,  $\Delta t$  is the time interval of each incremental step,  $\Delta\varepsilon^p$  is the plastic strain increment, and  $\vec{n}$  is the heat flow direction matrix.

Meanwhile, it is easy to know:

$$\begin{cases} \sigma = \frac{\partial W}{\partial \varepsilon^e} \\ \varepsilon = \varepsilon^e + \varepsilon^p + \varepsilon^T \\ \dot{\varepsilon}^p = D(\theta) \cdot \left(\frac{\bar{q}}{\sigma} - 1\right) \end{cases} \quad (7)$$

where  $W$  is the strain energy density, which is related to elastic strain and temperature,  $\varepsilon$  is the total strain,  $\varepsilon^e$  is the elastic strain,  $\varepsilon^p$  is the plastic strain,  $\varepsilon^T$  is the strain caused by thermal extension,  $D(\theta)$  is the material parameter related to temperature, and  $\bar{q}$  is Mises or Hill equivalent stress.

Incorporating Eq. (7) into Eq. (6), the relationship between the heat generated by plastic strain after the incremental step is obtained as Eq. (8):

$$\begin{cases} \partial\sigma = \frac{\partial^2 W}{\partial \varepsilon^e \partial \theta} \partial\theta + \frac{\partial^2 W}{\partial \varepsilon^e \partial \varepsilon^p} / \left(\partial\varepsilon - \frac{\partial\varepsilon^T}{\partial\theta} \partial\theta - \partial\varepsilon^p\right) \\ \partial\varepsilon^p = \partial\varepsilon^p \cdot \vec{n} + \Delta\varepsilon^p \left(\frac{\partial\vec{n}}{\partial\sigma} / \partial\sigma + \frac{\partial\vec{n}}{\partial\varepsilon^p} \partial\varepsilon^p + \frac{\partial\vec{n}}{\partial\theta} \partial\theta\right) \end{cases} \quad (8)$$

### 3.2 Equilibrium process of heat transfer and thermal-mechanical coupling

The heat generated during the grinding process is transferred to the inside of the material in the form of heat flow, as shown in Fig. 7. The heat flow vector  $\vec{q}$  entering the elastic medium through the system boundary causes changes in the internal energy and the volume expansion (increase temperature) or volume contraction (decrease temperature) of the material.

In Eq. (9), the heat flow vector  $\vec{q}$  replaces the entropy flux vector  $\vec{J}$ ,  $\rho\dot{s}$  is the time change rate of specific entropy per unit volume, and  $\rho\dot{h}$  is the time change rate of specific enthalpy per unit volume.

$$\begin{cases} \int_V \rho\dot{h} dV = \int_S \vec{q} \cdot \vec{n} dS \\ \int_S \vec{q} \cdot \vec{n} dS = \int_V \nabla \cdot \vec{q} dV \end{cases} \quad (9)$$

In rigid materials, the change of internal energy with time is used to replace the time enthalpy change, which includes the energy consumption of promoting the volume deformation and extrusion of the material under pressure. In order to determine the influence of thermal-mechanical coupling, the energy generation rate inside the material is temporarily ignored.

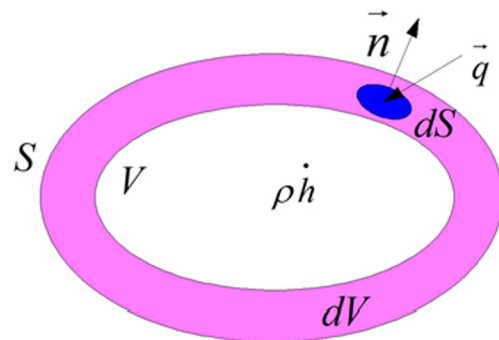


Fig. 7 Volume change caused by heat flow

Similarly, according to the divergence theorem, the surface integral is also related to the volume integral, which can be obtained by Eq. (9):

$$-\nabla \cdot \vec{q} = \rho \dot{h} \quad (10)$$

The negative sign reflects the direction of the heat flow vector opposite to the unit normal of the differential surface, as shown in Fig. 7. Finally, the equilibrium equation of thermal-mechanical coupling can be obtained through derivation (see Appendix 1 for the specific derivation process):

$$-\nabla \cdot \vec{q} = C_p \dot{T} \left( 1 + \eta \frac{\dot{\varepsilon}}{K_\varepsilon T} \right) \quad \text{with} \quad \eta = \frac{3KT_0 K_\varepsilon^2}{C_p} \quad (11)$$

where  $\eta$  is the thermal-mechanical coupling coefficient, a dimensionless quantity, which ensures the degree and process of thermal-mechanical coupling of the material;  $\frac{\dot{\varepsilon}}{K_\varepsilon T}$  is also dimensionless and is used to represent the ratio of the strain rate to the thermal strain rate.

As a general trend, thermal-mechanical coupling becomes more and more important in the transient process of materials, in which the stress-strain rate plays a promoting role in the load-time process.

### 3.3 Finite element equations of thermal-mechanical coupling for abrasive belt grinding

During the abrasive belt grinding process, the workpiece is squeezed by the abrasive belt grains to undergo elastic deformation. As the grinding progresses, the stress value becomes larger and larger. When the elastic limit of the workpiece material is exceeded, plastic deformation occurs. Simultaneously, as the elastoplastic deformation occurs, a large amount of grinding heat is generated by the friction between the wear debris-abrasive belt grain and the workpiece, and the corresponding increase in the grinding temperature causes the occurrence of thermal strain. Therefore, the total incremental strain  $d\varepsilon$  can be expressed as:

$$d\varepsilon = d\varepsilon^e + d\varepsilon^p + d\varepsilon^T \quad (12)$$

where  $d\varepsilon^e$ ,  $d\varepsilon^p$ , and  $d\varepsilon^T$  represent elastic strain differential, plastic strain differential, and thermal extension strain differential, respectively.

Therefore, the stress increment can be expressed by the following equation:

$$d\sigma = [D^e](d\varepsilon^e - d\varepsilon^p - d\varepsilon^T) \quad (13)$$

where  $[D^e]$  is the stress-strain matrix of the elastic deformation body and  $d\varepsilon^p$  is the derivative  $d\varepsilon^p = \lambda \frac{\partial f}{\partial \sigma}$  of the plastic potential  $f$ .

In order to simulate the influence of temperature, effective strain, and effective strain rate on the flow stress of the material, the optimal criterion of the model is also discussed and the flow stress equation of the material used is given in this study.

$$\bar{\sigma} = f(\bar{\varepsilon}, \dot{\bar{\varepsilon}}, T) \quad (14)$$

where  $\bar{\sigma}$  is the effective stress,  $\bar{\varepsilon}$  is the effective strain,  $\dot{\bar{\varepsilon}}$  is the effective strain rate, and  $T$  is the temperature.

Assuming that the material is hardened outward, based on the theory of large strain-large deformation, and using the modified Lagrangian equation and Prandtl-Reuss incremental theory, a thermal-elastoplastic constitutive equation considering strain rate and temperature is established:

$$d\sigma = [D^{ep}](d\varepsilon - d\varepsilon^T) + \frac{[D^e] \frac{\partial f}{\partial \sigma} \left( \frac{\partial R}{\partial \bar{\varepsilon}} d\bar{\varepsilon} + \frac{\partial R}{\partial T} dT \right)}{H' + \left( \frac{\partial f}{\partial \sigma} \right)^T [D^e] \frac{\partial f}{\partial \sigma}} \quad (15)$$

Finally, the relationship between nodal displacement and nodal force can be obtained through derivation when the Prandtl-Reuss flow law and thermal coupling coefficient are considered (see Appendix 2 for the specific derivation process):

$$\begin{cases} \{f\} = A[B]^T [D^e][B]\{u\} & \text{for } \sigma < \sigma_m \\ \{f_p\} = A[B]^T [D^{ep}][B]\{u\} + \int_{vol} [B]^T [D^{ep}] \frac{\sqrt{6}}{2} dW_T & \text{for } \sigma \geq \sigma_m \end{cases} \quad (16)$$

## 4 Thermal-mechanical coupling simulation of abrasive belt grinding

At present, for the thermal-mechanical coupling problem, the method of combining FE simulation and experiment is mostly used. Wan et al. [34] used Deform-3D to establish a thermal-mechanical coupling simulation model for zirconia grinding and simulated the subsurface damage, workpiece stress, and grinding temperature during the grinding process. The experimental results are basically consistent with the simulation results. Zheng et al. [35] used ANSYS to conduct a thermal-mechanical coupling simulation analysis on micro-deformed ball end mills, combined with theoretical calculations and milling experiments, and conducted an in-depth study on the thermal-mechanical coupling behavior of micro-deformed ball end mills during the grinding process. Olaogun et al. [36] established a thermal-mechanical coupling two-dimensional FE model, studied the thermal effect and friction coefficient of AA8015 aluminum alloy during industrial cold rolling, and predicted the temperature distribution of work

rolls. However, the abrasive belt grinding of titanium alloy is a very complex nonlinear dynamic grinding process. There are mutual coupling effects between multiple physical fields in the grinding process. Therefore, a more in-depth analysis of the coupling is conducted between the force field and the temperature field using ABAQUS software in the grinding process.

Abrasive belt grinding is completed by a large number of grains cutting edges arranged vertically on the surface of the abrasive belt. Each abrasive belt grain can be approximated as a miniature tool. Therefore, studying the grinding process of these single abrasive belt grains is the basis of studying the entire belt grinding. In this study, a simplified two-dimensional FE model of abrasive belt grain grinding is established by calculating the size and motion trajectory of the abrasive belt grain. Through the simulation of grinding force, grinding temperature, and material heat generation rate, the changing trend and law of grinding force, grinding temperature, and material heat generation during grinding are obtained, and the reasons for these changes are analyzed.

### 4.1 Abrasive belt grinding modeling and parameter design

#### 4.1.1 Analysis of abrasive belt surface morphology and abrasive belt grain movement

Under normal circumstances, the grains on the abrasive belt’s surface of the are implanted using static electricity or gravity. It is a single-layer-coated abrasive tool that can achieve compound grinding through multiple abrasive belt grains. Figure 8(a) is the pyramid alumina abrasive belt produced by 3M Company in the United States, and Fig. 8(b) is the

surface microtopography distribution of abrasive belt grains. Observed from the side, it can be seen that the abrasive belt grains are triangular. The sharp peaks of abrasive belt grains form grinding with the workpiece. This new type of grains makes the abrasive belt more efficient in removing material. It can be seen from Fig. 8(c) that the three-dimensional structure of the abrasive belt grains contains multiple layers of abrasive ore. Once the top of the pyramid is worn away, the next layer of new and sharp ore will take its place, ensuring the required grinding pressure.

Shown in Fig. 9 is the movement track of the grain removal material on the abrasive belt. When the abrasive belt is grinding, the abrasive belt grain is used as a fixed point on the abrasive belt. As the abrasive belt and the contact wheel rotate, the workpiece will perform a certain feed movement speed. From the kinematics point of view, the relative motion between a single abrasive belt grain and the workpiece to be ground can be transformed into an extended cycloid, and its trajectory equation is as follows:

$$\begin{cases} x = R_s \left( \sin\varphi \pm \frac{v_w}{60v_s}\varphi \right) \\ y = R_s(1 - \cos\varphi) \end{cases} \quad (17)$$

where  $R_s$  is the radius of the cutting circle, its value is the distance from the tip of the abrasive belt grain to the center of rotation, which is equal to the sum of the contact wheel radius  $R$ , the thickness  $d_b$  of the belt base, and the height  $h_s$  of the abrasive belt grain;  $\varphi$  is the angular displacement of the abrasive belt grain,  $\varphi \approx \sin\varphi \approx \frac{D}{R_s}$ ;  $D$  is the distance between the abrasive belt grains;  $v_s$  and  $v_w$  are the abrasive belt linear speed and the workpiece feed speed, respectively; “±” represents the processing method up grinding and down grinding. This study uses up grinding.

**Fig. 8** (a) Pyramid alumina abrasive belt; (b) surface microtopography distribution of abrasive belt grains; (c) wear of abrasive belt grains

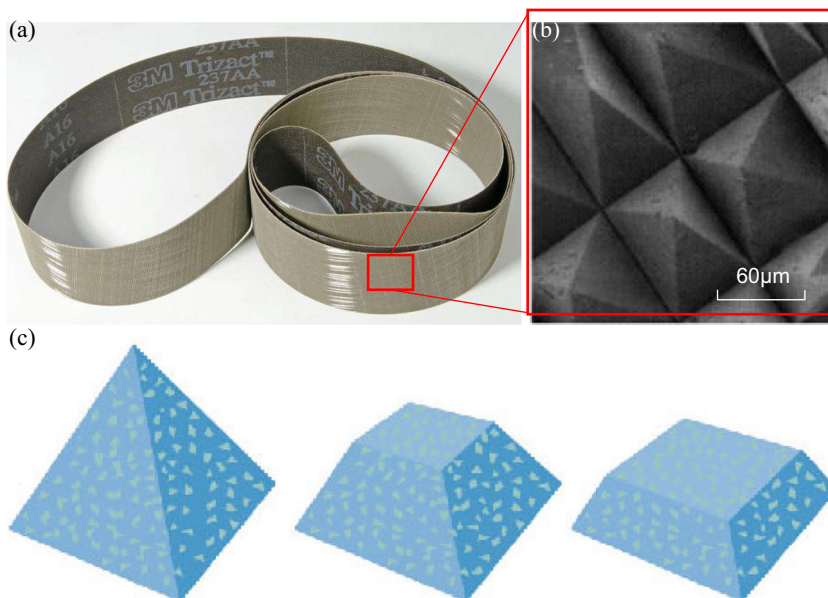
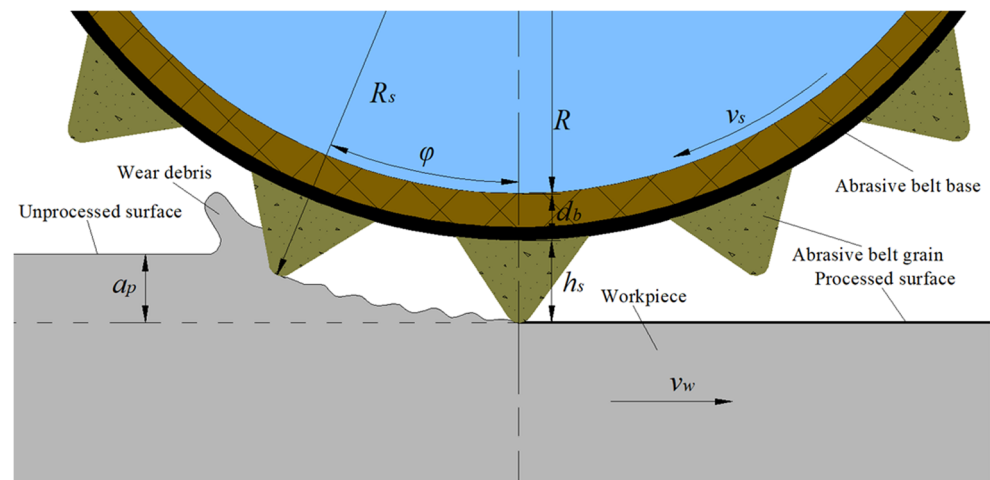


**Fig. 9** Abrasive belt grain removal material trajectory under microscopic size



It can be seen from Fig. 9 that the grinding trajectory of abrasive belt grain is similar to the direct parallel sliding grinding of grain, which is like removing material with a saw. Although the abrasive belt is a multi-edge grinding process, it is often the abrasive belt grain that first contacts the workpiece that undertakes the most grinding tasks. This abrasive belt grain is the first to remove the material, and the removal and polishing of elastic recovery part are carried out by subsequent grains grinding. Therefore, in order to simplify the model and calculation, the parallel movement of a single abrasive belt grain is directly considered when modeling, and it is used to grind the surface of the workpiece.

#### 4.1.2 Modeling and analysis of single abrasive belt grain

To simulate and analyze the grinding process, firstly, it is necessary to determine the most basic simulation model, grinding parameters, movement direction, etc. The simulation model includes geometric model and boundary load. According to the different actual machining physical processes, a grinding simulation model under different conditions is established. According to the observation of the morphology and distribution of grains on the abrasive belt's surface in the previous section, the size and trajectory of the abrasive belt grains are determined. Through simplification, a geometric model of single abrasive belt grain grinding is established for titanium alloy TC4, as shown in Fig. 10(a). The length of the processed workpiece is  $L = 1.1$  mm, and the height is  $H = 0.4$  mm. The front and back angles of the abrasive belt grain are both  $60^\circ$ , the apex angle is  $60^\circ$ , the height of abrasive belt grains is  $h_s = 0.06$  mm, and the abrasive belt grain moves in parallel along the grinding path to remove material, its speed  $V = v_s + v_w$ .

Metal grinding is a process of nonlinear and high strain rate, and the wear and jitter of abrasive belt grains will have

an impact. Therefore, the following simplifications should be made in establishing the FE model of the abrasive belt grinding process:

- (1) The casting defects are not considered, and the material is isotropic.
- (2) The jitter of abrasive belt grains and the movement perpendicular to the grinding plane are not considered.
- (3) The change of crystal structure on the workpiece surface is not considered due to temperature.
- (4) Due to the large difference in hardness between the two, the abrasive belt grains can be assumed to be rigid in contact, and the influence of geometric deformation is not considered.

Due to the grinding layer's main deformation, the node distance of the grinding layer is set to 0.005 mm. The two sides of the workpiece material under the grinding layer are offset in single-precision proportion according to the mesh node distance from 0.005 to 0.02 mm. The distance between the mesh nodes on the bottom edge of the workpiece is 0.02 mm. Considering the extrusion and grinding effect between the grain rake face and the workpiece, the distance between the abrasive rake face and the tip mesh node is set to 0.005 mm, and the flank face and the upper part of the grain are offset in single-precision proportion according to the mesh node distance from 0.005 to 0.02 mm. The 4-node plane strain nonlinear element is selected for mesh shape, and the dynamic temperature-displacement coupling (Dynamic, Temp-disp, Explicit) is selected for the element type. Figure 10(b) shows the FE mesh model. The total number of the workpiece mesh nodes is 11857, the total number of the workpiece mesh units is 11703, the total number of the grain mesh nodes is 138, and the total number of the grain mesh units is 115.

The entire simulation process is shown in Fig. 11.



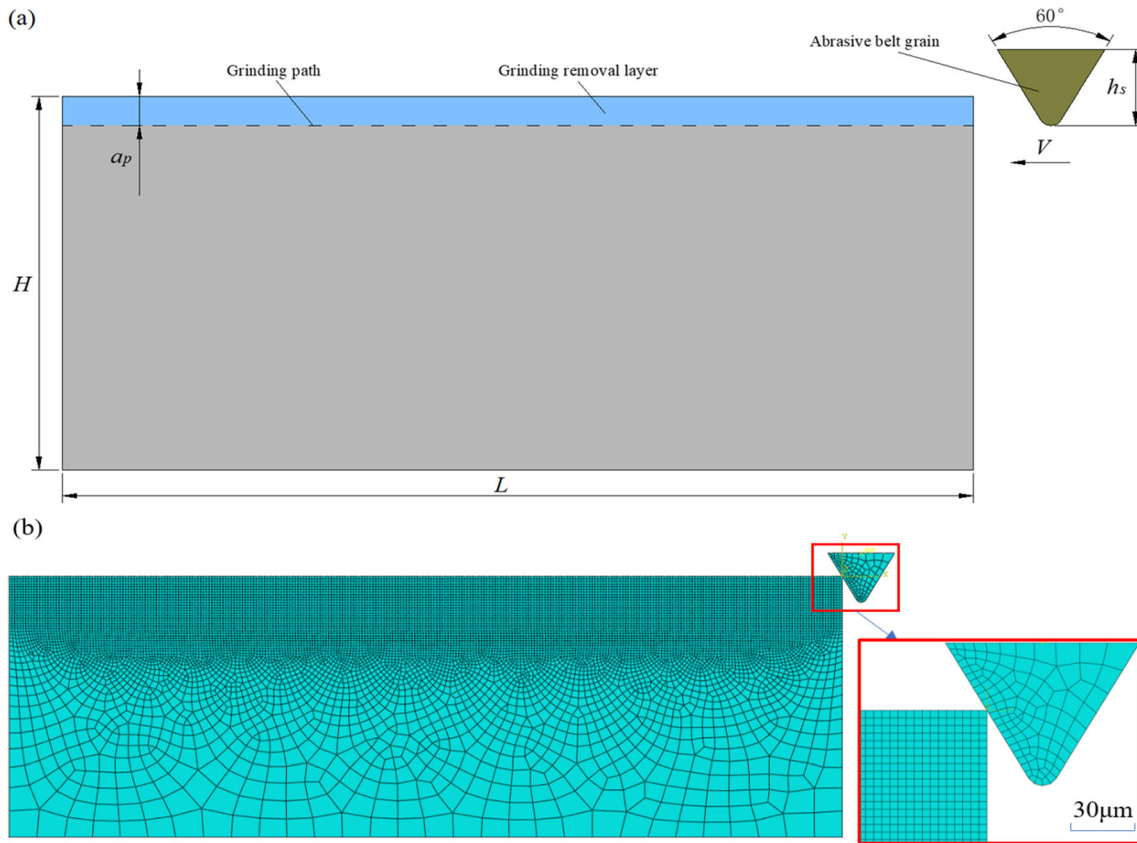


Fig. 10 (a) Geometry model of single abrasive belt grain grinding process; (b) FE mesh model of single abrasive belt grain grinding

### 4.2 Thermal-mechanical coupling simulation results and analysis

According to the simplification of the physical model and the establishment of the FE model in the previous section, the grinding process of single abrasive belt grain is simulated.

The grinding force, grinding temperature, and the deformation and heat generation of workpiece materials are analyzed and explained.

#### 4.2.1 Analysis of grinding stress field

Figure 12 is the stress distribution cloud diagram of the workpiece during the FE simulation process at different times when the grinding speed is  $V = 10$  m/s, and the grinding depth is  $a_p = 30 \mu\text{m}$ . It can be seen from Fig. 12 that in the grinding process, the stress in the I deformation zone (red zone) is very large, indicating that there is an obvious stress concentration in this zone. This is because the material in this deformation zone is under the continuous action of abrasive belt grains, and the material inside has a strong shear plastic deformation. In zone II, the equivalent stress of the material is relatively small, indicating that with the formation of continuous wear debris, the material in the area only undergoes corresponding translation. The wear debris is affected by the rake face of abrasive belt grains, and the material flows along the rake face of abrasive belt grains. A similar explanation has appeared in the literature [37].

As shown in Fig. 12, when the grinding process enters a steady state, the stress value distributed in the I deformation zone on the workpiece is the largest, and the stress value is

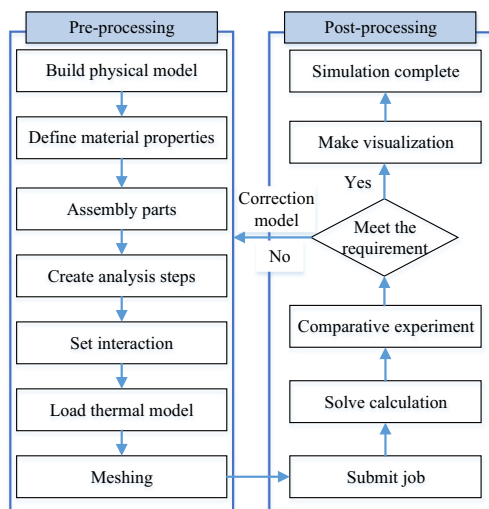
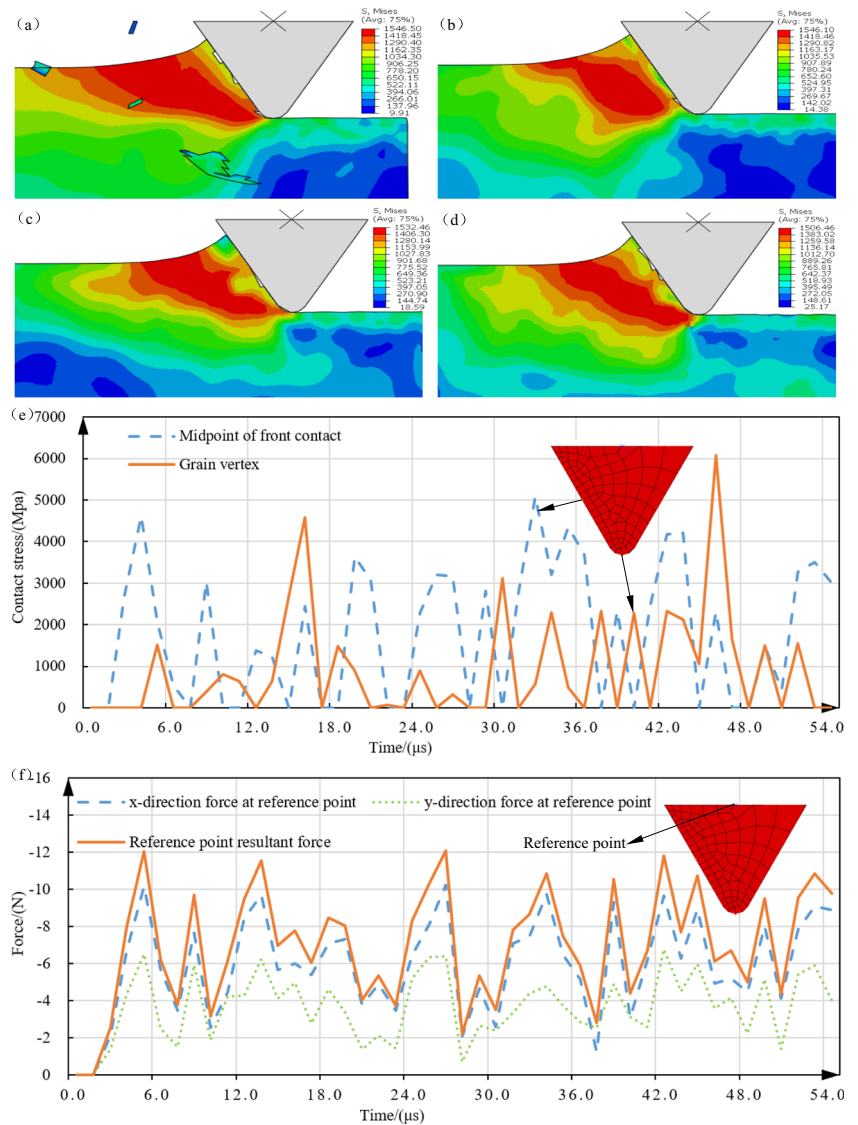


Fig. 11 Process of thermal-mechanical coupling simulation

**Fig. 12** Distribution of grinding stress (a)  $t = 13 \mu\text{s}$ , (b)  $t = 26 \mu\text{s}$ , (c)  $t = 39 \mu\text{s}$ , (d)  $t = 52 \mu\text{s}$ ; (e) change of contact stress at the midpoint of front contact of grain and the grain vertex with time; (f) change of grinding force at reference point with time



about 1546.50 MPa. As the grinding progresses, the maximum stress decreases slightly, and this change is almost negligible. The minimum stress is about 9.91 MPa, which appears far away from the grinding point. As the grinding progresses, the minimum stress shows an increasing trend.

Figure 12(e) shows the change of the contact stress between the midpoint of front contact of grain and the grain vertex with time. From Fig. 12(e), it can be seen that the contact stress occurs at the midpoint of front contact of grain first, and then the contact stress occurs at the grain vertex, which is more in line with reality. The contact stress at the midpoint of the front contact of the grain and the grain vertex shows certain fluctuations, and the trend is the same. But overall, the average contact stress at the midpoint of front contact of grain is greater than the average contact stress at the grain vertex. It also leads to the generation of large plastic strains. Figure 12(f) shows the grinding force at the reference

point of the grain. It can be known from Fig. 12(f) that during the entire grinding process, the grinding force at the reference point of grain is decomposed into the  $x$  and  $y$  directions, and the grinding forces in both directions show certain fluctuations, and the trends are consistent. But overall, the grinding force in the  $x$  direction is greater than the grinding force in the  $y$  direction (the grinding force in the  $x$  direction is about 6.3 N, and the grinding force in the  $y$  direction is about 3.0 N). This is because the  $x$  direction mainly performs the removal of grinding materials, so the grinding force is greater, which is more in line with reality. In the initial stage of grinding, when the abrasive belt grain just starts to cut in, the workpiece material begins to undergo elastoplastic deformation, and the contact zone between the two is also increasing. The grinding force increases rapidly from 0. As the grinding becomes stable, the average value is stable at around 7.0 N, which is also more consistent with the actual grinding situation.

#### 4.2.2 Analysis of grinding strain field

Figure 13 shows the equivalent plastic strain distribution nephogram and the maximum principal stress distribution nephogram of the workpiece when the grinding speed is  $V = 10$  m/s, the grinding depth is  $a_p = 30$   $\mu\text{m}$ , and the grinding time is  $t = 13$   $\mu\text{s}$ . The equivalent plastic strain is also mainly concentrated in the I deformation zone, the machined surface, and the abrasive belt grain-wear debris contact zone. The maximum equivalent plastic strain appears in the abrasive belt grain-wear debris contact zone, and the maximum equivalent plastic strain value is 0.948. The reason is that the workpiece material is sheared and fibrillated in the I deformation zone. As the grinding progresses, this part of the metal material enters the II deformation zone, and then it rubs against the rake face of grain and is squeezed; the fibrosis is further deepened, so the equivalent plastic strain is the largest (The red elliptical zone as shown in Fig. 13(a)). As we can see from Fig. 13(b), the equivalent plastic strain (Fig. 13(a)) and temperature (Fig. 14(a, b, c, d, e, and f)) of the material near the midpoint of front contact of grain are higher than other areas, thereby forming a thermal softening zone. Near the midpoint of front contact of grain, there is compressive stress, while the outer surface of wear debris is tensile stress. Under the action of this outer surface tensile stress, the concentration of plastic slip in the main shear zone is further deepened so that flake wear debris and granular wear debris are formed.

#### 4.2.3 Analysis of grinding temperature field and wear debris formation

Figure 14 shows the temperature distribution of the workpiece and the formation of wear debris in the FE simulation process at different times when the grinding speed is  $V = 10$  m/s, and the grinding depth is  $a_p = 30$   $\mu\text{m}$ . It can be seen from Fig. 14 that during the formation of wear debris, the abrasive belt grain begins to move at a specified speed. As the grinding progresses, the ground material is separated from the workpiece, and the workpiece material is divided into two parts under the action of the abrasive belt grain. Partly due to the shear slip under the action of the abrasive belt grain, along the

depth of the abrasive belt grain, the material flows out along the rake face of the abrasive belt grain. The corresponding flake and granular wear debris are also produced (as shown in Fig. 14(b) and (c)); the other part remains on the machined surface. It can be seen from Fig. 14(a, b, c, d, and e) that as the grinding progresses, the heat-affected zone in the abrasive belt grain continues to increase, and a similar phenomenon occurs in literature [38, 39].

It can be seen from Fig. 14 that due to the constant friction between the rake face of abrasive belt grain and the wear debris, the heat generated also increases accordingly. In addition to the heat generated in the I deformation zone, the highest grinding temperature is generated in the friction area between the rake face and wear debris (about 500.85  $^{\circ}\text{C}$ ). Figure 14(f) shows the temperature change of contact area with time at the midpoint of front contact of abrasive belt grain and the grain vertex. At the beginning of the grinding process, the temperature rises sharply because the abrasive belt grain just contacted the workpiece. As the grinding progresses, the upward trend is slowing down at about 6  $\mu\text{s}$  and finally tends to a stable state.

#### 4.2.4 Coupling analysis of grinding temperature field and force field

Figure 15 shows the relationship between the contact stress and temperature in the grinding process with time. During the entire grinding process, as the grinding process progresses, the temperature tends to stabilize (the grain vertex temperature is about 450  $^{\circ}\text{C}$ , and the midpoint temperature of front contact of grain is about 475  $^{\circ}\text{C}$ ), and the contact stress tends to a stable floating (the grain vertex contact stress of grain is about 950 MPa, and the midpoint contact stress of front contact of grain is about 1500 MPa). This rule is more obvious in Fig. 15(b) than Fig. 15(a); that is, the temperature and contact stress at the midpoint of front contact of grain are more stable. Simultaneously, when the temperature and contact stress stabilize, the equivalent maximum stress concentration area hardly expands (Fig. 12(b, c, and d)), and it also tends to stabilize.

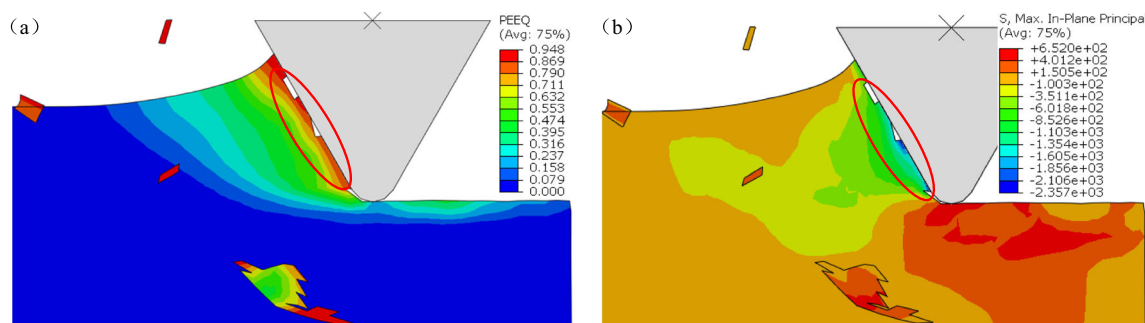
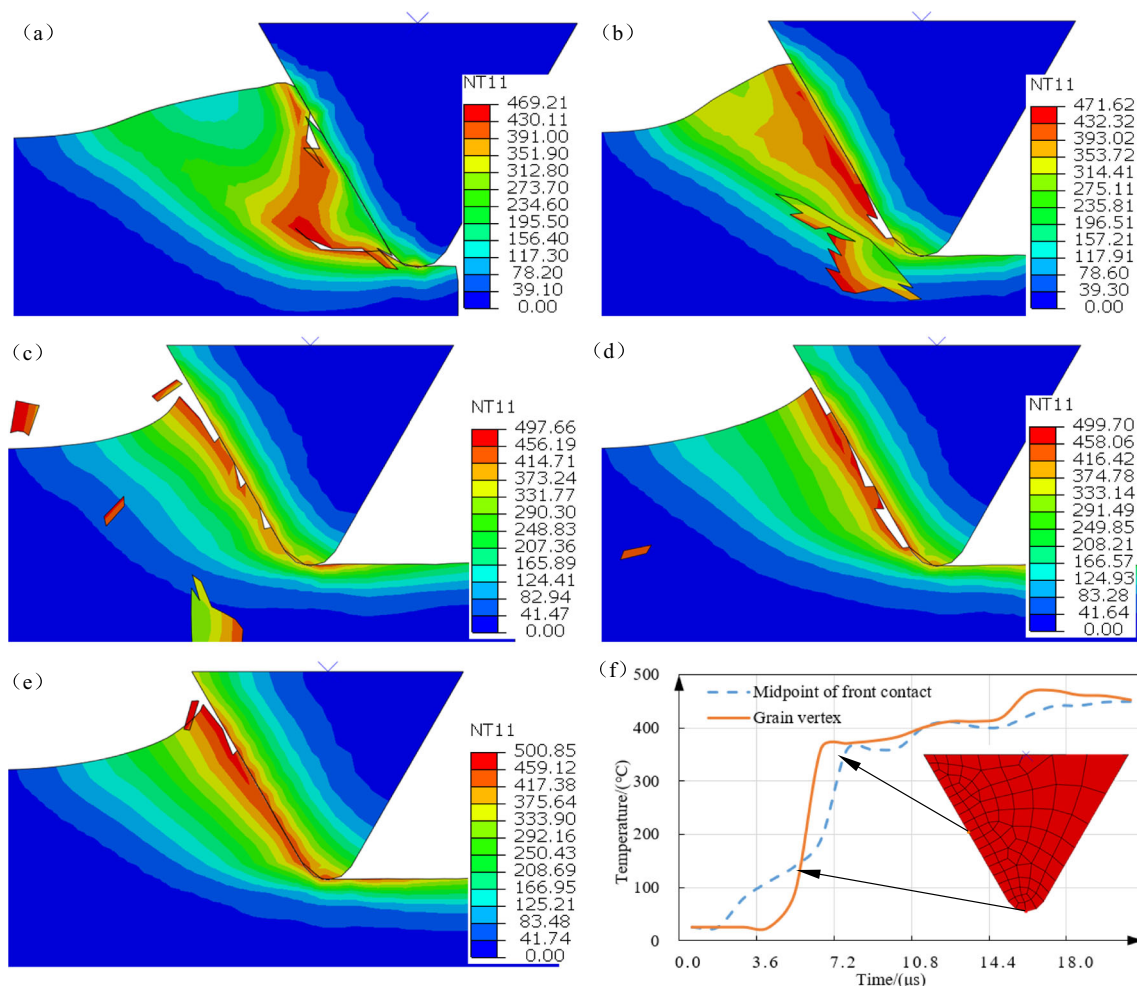


Fig. 13 (a) Grinding equivalent plastic strain distribution nephogram. (b) Maximum principal stress distribution nephogram



**Fig. 14** Grinding temperature distribution (a)  $t = 6 \mu\text{s}$ , (b)  $t = 8 \mu\text{s}$ , (c)  $t = 11 \mu\text{s}$ , (d)  $t = 15 \mu\text{s}$ , (e)  $t = 20 \mu\text{s}$ ; (f) the temperature change of the grain vertex and the midpoint of front contact

## 5 Discussion

During the experimental measurement of grinding force, when the grinding has not yet started, the data measured has already appeared fluctuations by the dynamometer, so when the grinding is over, it is particularly important to choose a suitable filtering and noise reduction method. This study uses the Savitzky-Golay algorithm to filter, which not only preserves the shape and width of the original signal but also achieves filtering and noise reduction, showing good consistency, as shown in Fig. 3. In the process of measuring grinding temperature, another special phenomenon is found. As the grinding progresses, the maximum temperature of the ground surface gradually decreases from Fig. 4(a1)→(b1)→(c1), the corresponding temperature dropped from 52.95 to 43.30 °C. The reason for this phenomenon has not been seen in other reports.

During the simulation process of grinding force, the I deformation zone is found, and obvious stress concentration is

found in this area as shown in Fig. 12(a, b, c, and d), which is more consistent with the previous theoretical analysis, the deformation zone shown in Fig. 5. In the grinding process, due to the large negative rake angle of abrasive belt grain, a dead metal zone is formed before the rake face of the grain, as shown in Fig. 14(b) and (d). This simulation result is consistent with the result of the literature [40]. In the simulation process of grinding temperature, as the grinding progresses, the heat-affected zone inside the abrasive belt grain continues to expand, and the heat-affected area of the external rake face of abrasive belt grain tends to be stable, as shown in Fig. 14(b, c, d, and e).

## 6 Conclusion

This study takes the thermal-mechanical coupling problem as the research object in the abrasive belt grinding process and conducts the thermal-mechanical measurement experiment in



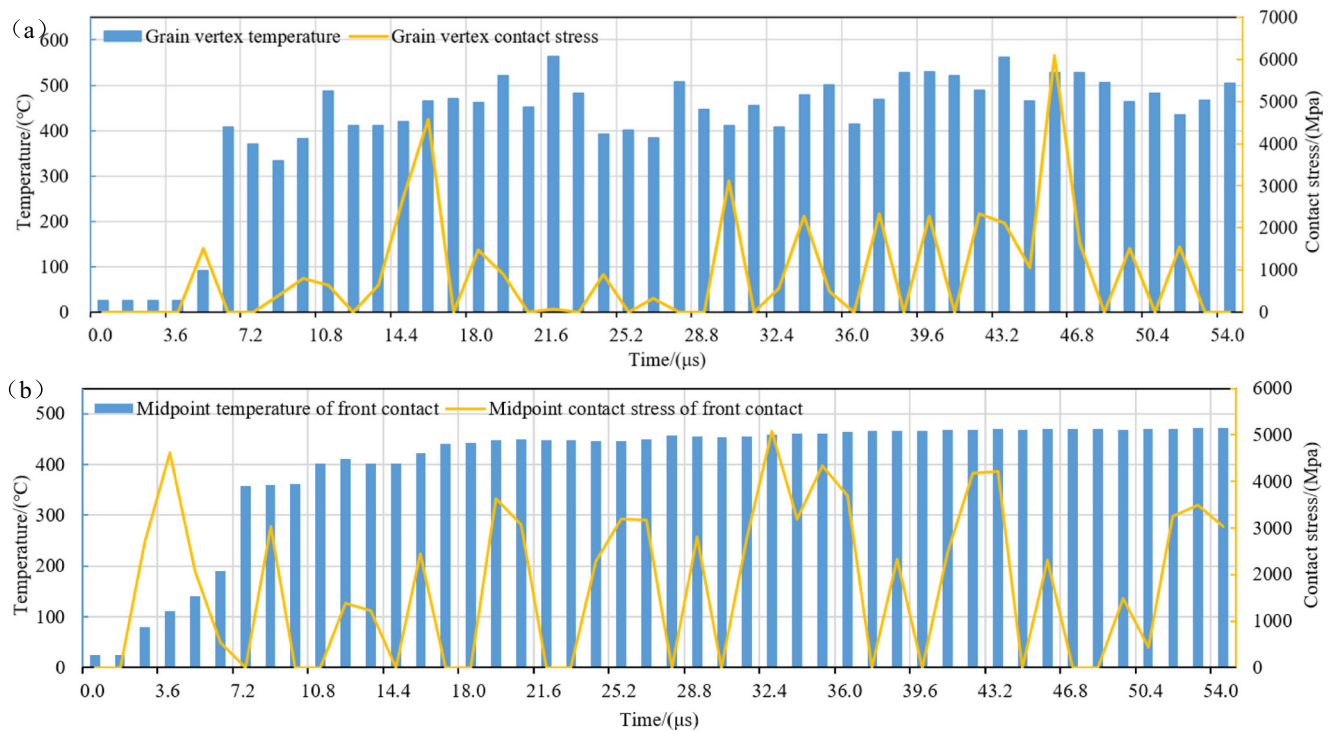


**Fig. 15** Relationship between the contact stress and temperature change with time during the grinding process. (a) Grain vertex; (b) midpoint of front contact of grain

the abrasive belt grinding process. The thermal-mechanical coupling theory of abrasive belt grinding is discussed in detail. The simulation analysis of single particle grinding of abrasive belt grinding is carried out and discussed in combination with actual problems. The main conclusions are as follows:

- (1) The Savitzky-Golay filtering is performed by using MATLAB. The results show that the entire grinding process is divided into grinding contact stage, grinding stable stage, and grinding exit stage. The grinding force in the  $x$  and  $y$  directions in the grinding stable stage is 6.1 N and 2.8 N, respectively.
- (2) During the monitoring of the grinding temperature, with the progress of the grinding experiment, the surface temperature of the workpiece dropped from 52.95 to 43.30 °C, showing a downward trend, which is not found in previous studies.
- (3) The plastic deformation zone appeared in the grinding simulation process, which is more consistent with the previous theoretical research. During the simulation, the temperature-affected zone of the grinding tends to be stable. In addition, with the grinding simulation progress, a dead metal zone is found before the rake face of the abrasive belt grain.

This study analyzes the thermal-mechanical problems of the abrasive belt grinding process from the perspectives of experiment, theory, and simulation. The related methods can

be used in other processing, such as turning, milling, and wheel grinding. In the future, this work can further study the thermal-mechanical optimization and the effect of thermal-mechanical on the surface integrity of the workpiece.

**Authors' contributions** Kangkang Song: Investigation, methodology, writing original draft, and visualization. Guijian Xiao: Funding acquisition, project administration, resources, supervision, and validation. Shulin Chen: Data curation, software, and conceptualization. Shaochuan Li: Experiment, writing review, and editing.

**Funding** The authors gratefully acknowledge the financial support for this work by the National Natural Science Foundation of China under Grant (No. U1908232), the National Science and Technology Major Project (No. 2017-VII-0002-0095), and the Graduate Scientific Research and Innovation Foundation of Chongqing (No. CYB20009).

**Data availability** The datasets used or analyzed during the current study are available from the corresponding author on reasonable request.

### Compliance with ethical standards

**Competing interests** The authors declare that they have no known competing financial interests or personal relationships that could have appeared to influence the work reported in this paper.

**Ethical approval** Ethical approval was not required for this study.

**Consent to participate** Written informed consent was obtained from individual or guardian participants.

**Consent to publish** Manuscript was approved by all authors for publication.

## Appendix 1. Derivation of the thermal-mechanical coupling equilibrium equation

In Eq. (10), for rigid materials, specific enthalpy is a function of temperature; for deformable materials, specific enthalpy is a function of temperature and material volume increase, which can be expressed mathematically as:

$$h \equiv h(T, e), \quad \text{with } e = e_{11} + e_{22} + e_{33} \quad (18)$$

where  $e_{ij}$  is the Cauchy strain tensor. The sum of its three normal components is defined for the volume change of a deformable object. Therefore, the time change rate of specific enthalpy is:

$$\rho \dot{h} = \rho \left( \frac{\partial h}{\partial T} \right)_e \dot{T} + \rho \left( \frac{\partial h}{\partial e} \right)_T \dot{e} \quad (19)$$

In classical thermodynamics, the first term  $\rho \left( \frac{\partial h}{\partial T} \right)_e$  is considered the volumetric specific heat capacity  $C_p$  under constant pressure, and the second term  $\rho \left( \frac{\partial h}{\partial e} \right)_T$  can be defined as another type of specific heat capacity  $C_k$ , which measures the energy required for the isothermal volume change per unit volume of the continuum. The volume change of the continuum is caused by the strain generated by force. The specific heat capacity  $C_k$  is the bridge between mechanical deformation and heat generation. Like the volume specific heat, the specific heat capacity  $C_k$  is a function of temperature. Expand the equation according to the Taylor series as follows:

$$\rho \left( \frac{\partial h}{\partial e} \right)_T \equiv C_k(T) \equiv C_k(T_0) + \left( \frac{\partial C_k}{\partial T} \right)_{T_0} (T - T_0) + \dots \quad (20)$$

The specific heat capacity  $C_k$  is at the reference temperature point. In order to make the coefficient of thermal expansion used in the contact linear thermoelastic theory zero without losing generality, and assuming that the temperature change  $T - T_0$  is the same order of magnitude as the reference temperature  $T_0$ , Eq. (20) can be simplified as follows:

$$\rho \left( \frac{\partial h}{\partial e} \right)_T \cong \left( \frac{\partial C_k}{\partial T} \right)_{T_0} T_0 \quad (21)$$

Substituting Eq. (21) into Eq. (19), the time change rate of specific enthalpy per unit volume is as follows:

$$\rho \dot{h} = C_p \dot{T} + \left( \frac{\partial C_k}{\partial T} \right)_{T_0} T_0 \dot{e}, \quad \text{with } \left( \frac{\partial C_k}{\partial T} \right)_0 \equiv \left( \frac{\partial C_k}{\partial T} \right)_{T_0} \quad (22)$$

Finally, substituting Eq. (22) into Eq. (10), we can get:

$$-\nabla \cdot \vec{q} = C_p \dot{T} + K_\sigma T_0 \dot{e}, \quad K_\sigma \equiv \left( \frac{\partial C_k}{\partial T} \right)_0 \quad (23)$$

Another form of simplification and deformation of Eq. (23) can be obtained:

$$\begin{aligned} -\nabla \cdot \vec{q} &= C_p \dot{T} \left( \frac{1 + K_\sigma T_0 e}{C_p \dot{T}} \right) \\ &= C_p \dot{T} \left[ 1 + \frac{3KT_0 K_\varepsilon^2}{C_p} \left( \frac{\dot{e}}{K_\varepsilon \dot{T}} \right) \right] \end{aligned} \quad (24)$$

Equation (24) is normalized to obtain the following results:

$$-\nabla \cdot \vec{q} = C_p \dot{T} \left( 1 + \eta \frac{\dot{e}}{K_\varepsilon \dot{T}} \right) \quad \text{with } \eta = \frac{3KT_0 K_\varepsilon^2}{C_p} \quad (25)$$

where  $\eta$  is the thermal-mechanical coupling coefficient, a dimensionless quantity, which ensures the degree and process of thermal-mechanical coupling of the material ( $3K \cdot K_\varepsilon = K_\sigma$ );  $\frac{\dot{e}}{K_\varepsilon \dot{T}}$  is also dimensionless and is used to represent the ratio of the strain rate to the thermal strain rate.

## Appendix 2. Derivation of the relationship between nodal displacement and nodal force

In Eq. (15),  $\dot{H}$  is the strain hardening rate, and the expression of elastoplastic stress-strain matrix  $[D^{ep}]$  is as follows:

$$[D^{ep}] = [D^e] - \frac{[D^e] \frac{\partial f}{\partial \sigma} \left( \frac{\partial f}{\partial \sigma} \right)^T [D^e]}{H' + \left( \frac{\partial f}{\partial \sigma} \right)^T [D^e] \frac{\partial f}{\partial \sigma}} \quad (26)$$

If the entire deformation process is elastic, then the elastic stress-strain matrix  $[D^e]$  can be directly used instead of the elastic-plastic stress-strain matrix  $[D^{ep}]$  to solve the elastic deformation. The stress component  $\frac{\partial f}{\partial \sigma}$  is obtained by using the expression of plastic potential  $f$ . From the above derivation, the stress-strain relationship of plane strain deformation can be derived as follows.

(1) Elastic stage

$$d\sigma = [D^e] (d\varepsilon - d\varepsilon^T) \quad (27)$$

(2) Plastic stage

$$d\sigma = [D^{ep}](d\varepsilon - d\varepsilon^T) + \frac{2}{3} \frac{\bar{\sigma}\{S\}}{S_0} \left( \frac{\partial R}{\partial \bar{\varepsilon}} d\bar{\varepsilon} + \frac{\partial R}{\partial T} dT \right) \quad (28)$$

where

$$\{S\} = [D^e] \{ \sigma' \} \quad (29)$$

$$S_0 = \frac{4}{9} (\bar{\sigma})^2 H' + \{ \sigma' \}^T \{ S \} \quad (30)$$

where  $\sigma'$  is the stress deflection tensor.

The Prandtl-Reuss flow law is considered; the corresponding strain-specific energy increment is:

$$dW = \sigma_{ij} d\varepsilon_{ij} = (\sigma_m \delta_{ij} + S_{ij})(d\varepsilon_m \delta_{ij} + de_{ij}) \quad (31)$$

By expanding and simplifying the above equation, the following result is obtained:

$$dW = \sigma_m d\varepsilon_m \delta_{ij} \delta_{ij} + d\varepsilon_m S_{ij} \delta_{ij} + de_{ij} \sigma_m \delta_{ij} + de_{ij} S_{ij} = 3\sigma_m d\varepsilon_m + de_{ij} S_{ij} \quad (32)$$

where  $3\sigma_m d\varepsilon_m$  is the volumetric specific energy increment of the material,  $de_{ij} S_{ij}$  is the temperature deformation specific energy of the material, denoted as  $W_T$ , and then the material shape specific energy in the differential form can be expressed as Eq. (33), where  $S_{ij} dS_{ij} = 0$ ,  $S_{ij} S_{ij} = \frac{2}{3} \sigma_i^2$ .

$$dW_T = de_{ij} S_{ij} = S_{ij} \left( \frac{1}{2G} dS_{ij} + S_{ij} d\lambda \right) = \frac{1}{2G} S_{ij} dS_{ij} + S_{ij} S_{ij} d\lambda = \frac{2}{3} \sigma_i^2 d\lambda \quad (33)$$

Simultaneous Eqs. (26), (27), (28), and (33), and take its integral form. When the Prandtl-Reuss flow law and thermal-mechanical coupling coefficient are considered, the nodal displacement and the nodal force relationship is obtained:

$$\begin{cases} \{f\} = A[B]^T [D^e][B]\{u\} & \text{for } \sigma < \sigma_m \\ \{f_p\} = A[B]^T [D^{ep}][B]\{u\} + \int_{vol} [B]^T [D^{ep}] \frac{\sqrt{6}}{2} dW_T & \text{for } \sigma \geq \sigma_m \end{cases} \quad (34)$$

## References

1. Qian N, Fu Y, Zhang Y, Chen J, Xu J (2019) Experimental investigation of thermal performance of the oscillating heat pipe for the grinding wheel. *Int J Heat Mass Transf* 136:911–923. <https://doi.org/10.1016/j.ijheatmasstransfer.2019.03.065>
2. Yang H, Ding W, Chen Y, Laporte S, Xu J, Fu Y (2019) Drilling force model for forced low frequency vibration assisted drilling of Ti-6Al-4V titanium alloy. *Int J Mach Tools Manuf* 146. <https://doi.org/10.1016/j.ijmachtools.2019.103438>

3. Xi X, Ding W, Wu Z, Anggei L (2020) Performance evaluation of creep feed grinding of  $\gamma$ -TiAl intermetallics with electroplated diamond wheels. *Chin J Aeronaut*. <https://doi.org/10.1016/j.cja.2020.04.031>
4. Fan W, Wang W, Wang J, Zhang X, Qian C, Ma T (2020) Microscopic contact pressure and material removal modeling in rail grinding using abrasive belt. *Proc Inst Mech Eng B J Eng Manuf* 235:3–12. <https://doi.org/10.1177/0954405420932419>
5. Huang Y, He S, Xiao G, Li W, Jiahua S, Wang W (2020) Effects research on theoretical-modelling based suppression of the contact flutter in blisk belt grinding. *J Manuf Process* 54:309–317. <https://doi.org/10.1016/j.jmapro.2020.03.021>
6. Wu X, Gao Z, Meng H, Wang Y, Cheng C (2020) Experimental study on the uniform distribution of gas-liquid two-phase flow in a variable-aperture deflector in a parallel flow heat exchanger. *Int J Heat Mass Transf* 150. <https://doi.org/10.1016/j.ijheatmasstransfer.2020.119353>
7. Li B, Dai C, Ding W, Yang C, Li C, Kulik O, Shumyacher V (2020) Prediction on grinding force during grinding powder metallurgy nickel-based superalloy FGH96 with electroplated CBN abrasive wheel. *Chin J Aeronaut*. <https://doi.org/10.1016/j.cja.2020.05.002>
8. Xiao G, He Y, Huang Y, He S, Wang W, Wu Y (2020) Bionic microstructure on titanium alloy blade with belt grinding and its drag reduction performance. *Proc Inst Mech Eng B J Eng Manuf*: 095440542094974. <https://doi.org/10.1177/0954405420949744>
9. Li C, Li X, Wu Y, Zhang F, Huang H (2019) Deformation mechanism and force modelling of the grinding of YAG single crystals. *Int J Mach Tools Manuf* 143:23–37. <https://doi.org/10.1016/j.ijmachtools.2019.05.003>
10. Wang W, Salvatore F, Rech J (2020) Characteristic assessment and analysis of residual stresses generated by dry belt finishing on hard turned AISI52100. *J Manuf Process* 59:11–18. <https://doi.org/10.1016/j.jmapro.2020.09.039>
11. Xiao G, Zhang Y, Huang Y, Song S, Chen B (2021) Grinding mechanism of titanium alloy: research status and prospect. *J Adv Manuf Sci Technol* 1(1):2020001. <https://doi.org/10.51393/j.jamst.2020001>
12. Feng SZ, Cui XY, Li AM (2016) Fast and efficient analysis of transient nonlinear heat conduction problems using combined approximations (CA) method. *Int J Heat Mass Transf* 97:638–644. <https://doi.org/10.1016/j.ijheatmasstransfer.2016.02.061>
13. Liu S, Lin M (2019) Thermal-mechanical coupling analysis and experimental study on CNC machine tool feed mechanism. *Int J Precis Eng Manuf* 20(6):993–1006. <https://doi.org/10.1007/s12541-019-00069-1>
14. Huang J, Yuan J, Wang Z (2017) Influence of thermal-mechanical coupling effect on vibration of double-drive feed system. *Int J Heat Technol* 35:177–182. <https://doi.org/10.18280/ijht.350123>
15. Wu C, Ji C, Zhu M (2019) Influence of differential roll rotation speed on evolution of internal porosity in continuous casting bloom during heavy reduction. *J Mater Process Technol* 271:651–659. <https://doi.org/10.1016/j.jmatprotec.2019.04.041>
16. Chakraborty S, Ganguly S, Talukdar P (2019) Determination of optimal taper in continuous casting billet mould using thermo-mechanical models of mould and billet. *J Mater Process Technol* 270:132–141. <https://doi.org/10.1016/j.jmatprotec.2019.02.032>
17. Soundararajan V, Zekovic S, Kovacevic R (2005) Thermo-mechanical model with adaptive boundary conditions for friction stir welding of Al 6061, *International Journal of Machine Tools and Manufacture*. 45(14):1577–1587. <https://doi.org/10.1016/j.ijmachtools.2005.02.008>
18. Wang Z, Zhang X, Chen J (2020) An effective thermal-mechanical coupling method for simulating friction stir-assisted incremental aluminum alloy sheet forming. *Int J Adv Manuf Technol* 107(7-8):3449–3458. <https://doi.org/10.1007/s00170-020-05286-x>

19. Lu X, Wang H, Jia Z, Feng Y, Liang SY (2018) Coupled thermal and mechanical analyses of micro-milling Inconel 718. *Proc Inst Mech Eng B J Eng Manuf* 233(4):1112–1126. <https://doi.org/10.1177/0954405418774586>
20. Guiju Z, Caiyuan X (2019) Analysis of thermal stress distribution of TBM disc cutter. *Aust J Mech Eng* 16(sup1):43–48. <https://doi.org/10.1080/1448837x.2018.1545471>
21. Jiang B, Yang W, Zhang Z, Li X, Ren X, Wang Y (2020) Numerical simulation and experiment of electrically-assisted incremental forming of thin TC4 titanium alloy sheet. *Mater (Basel)* 13(6). <https://doi.org/10.3390/ma13061335>
22. Li H, Shin YC (2004) Analysis of bearing configuration effects on high speed spindles using an integrated dynamic thermo-mechanical spindle model. *Int J Mach Tools Manuf* 44(4):347–364. <https://doi.org/10.1016/j.ijmactools.2003.10.011>
23. Farias RM, Teixeira PRF, Araújo DB (2016) Thermo-mechanical analysis of the MIG/MAG multi-pass welding process on AISI 304 L stainless steel plates. *J Braz Soc Mech Sci Eng* 39(4):1245–1258. <https://doi.org/10.1007/s40430-016-0574-y>
24. Zhang H, Xu W, Xu Y, Lu Z, Li D (2018) The thermal-mechanical behavior of WTaMoNb high-entropy alloy via selective laser melting (SLM): experiment and simulation. *Int J Adv Manuf Technol* 96(1–4):461–474. <https://doi.org/10.1007/s00170-017-1331-9>
25. Motaman SAH, Schacht K, Haase C, Prah U (2019) Thermo-micro-mechanical simulation of metal forming processes. *Int J Solids Struct* 178–179:59–80. <https://doi.org/10.1016/j.ijsolstr.2019.05.028>
26. Ji H, Dong J, Xin L, Huang X, Liu J (2018) Numerical and experimental study on the thermodynamic coupling of Ti-6Al-4V blade preforms by cross wedge rolling. *Metals* 8(12). <https://doi.org/10.3390/met8121054>
27. Liu J, Wang Y, Li H, Costil S, Bolot R (2017) Numerical and experimental analysis of thermal and mechanical behavior of NiCrBSi coatings during the plasma spray process. *J Mater Process Technol* 249:471–478. <https://doi.org/10.1016/j.jmatprotec.2017.06.025>
28. Zhu D, Feng X, Xu X, Yang Z, Li W, Yan S, Ding H (2020) Robotic grinding of complex components: a step towards efficient and intelligent machining – challenges, solutions, and applications. *Robot Comput Integr Manuf* 65. <https://doi.org/10.1016/j.rcim.2019.101908>
29. Wang B, Liu Z (2015) Shear localization sensitivity analysis for Johnson–Cook constitutive parameters on serrated chips in high speed machining of Ti6Al4V. *Simul Model Pract Theory* 55:63–76. <https://doi.org/10.1016/j.simpat.201503.011>
30. Zhang X, Chen H, Xu J, Song X, Wang J, Chen X (2018) A novel sound-based belt condition monitoring method for robotic grinding using optimally pruned extreme learning machine. *J Mater Process Technol* 260:9–19. <https://doi.org/10.1016/j.jmatprotec.2018.05.013>
31. Ma Y, Feng P, Zhang J, Wu Z, Yu D (2016) Prediction of surface residual stress after end milling based on cutting force and temperature. *J Mater Process Technol* 235:41–48. <https://doi.org/10.1016/j.jmatprotec.2016.04.002>
32. Voyiadjis GZ, Palazotto AN, Al-Rub RKA (2008) Constitutive modeling and simulation of perforation of targets by projectiles. *AIAA J* 46(2):304–316. <https://doi.org/10.2514/1.26011>
33. Ghazanfarian J, Shomali Z, Abbassi A (2015) Macro- to nanoscale heat and mass transfer: the lagging behavior. *Int J Thermophys* 36(7):1416–1467. <https://doi.org/10.1007/s10765-015-1913-4>
34. Wan L, Li L, Deng Z, Deng Z, Liu W (2019) Thermal-mechanical coupling simulation and experimental research on the grinding of zirconia ceramics. *J Manuf Process* 47:41–51. <https://doi.org/10.1016/j.jmapro.2019.09.024>
35. Zheng M, He C, Yang S (2020) Thermo-mechanical coupling behaviour when milling titanium alloy with micro-textured ball-end cutters. *Proc Inst Mechan Eng E: J Proc Mechan Eng* 234(6):562–575. <https://doi.org/10.1177/0954408920931958>
36. Olaogun O, Edberg J, Lindgren LE, Oluwole OO, Akinlabi ET (2018) Heat transfer in cold rolling process of AA8015 alloy: a case study of 2-D FE simulation of coupled thermo-mechanical modeling. *Int J Adv Manuf Technol* 100(9–12):2617–2627. <https://doi.org/10.1007/s00170-018-2811-2>
37. Zhang Y, Li C, Ji H, Yang X, Yang M, Jia D, Zhang X, Li R, Wang J (2017) Analysis of grinding mechanics and improved predictive force model based on material-removal and plastic-stacking mechanisms. *Int J Mach Tools Manuf* 122:81–97. <https://doi.org/10.1016/j.ijmactools.2017.06.002>
38. Kunderák J, Markopoulos AP, Karkalos NE (2017) Numerical simulation of grinding with realistic representation of grinding wheel and workpiece movements: a finite volumes study. *Procedia CIRP* 58:275–280. <https://doi.org/10.1016/j.procir.2017.03.192>
39. Su J, Ke Q, Deng X, Ren X (2018) Numerical simulation and experimental analysis of temperature field of gear form grinding. *Int J Adv Manuf Technol* 97(5–8):2351–2367. <https://doi.org/10.1007/s00170-018-2079-6>
40. Jamshidi H, Budak E (2020) An analytical grinding force model based on individual grit interaction. *J Mater Process Technol*:283. <https://doi.org/10.1016/j.jmatprotec.2020.116700>

**Publisher's note** Springer Nature remains neutral with regard to jurisdictional claims in published maps and institutional affiliations.